Supporting Information

Jasnin et al. 10.1073/pnas.1320155110

SI Text

Bacterial Strains, Mammalian Cells, and Culture Conditions. *Listeria monocytogenes* strain EGD (BUG 600) was grown overnight at 37 °C in brain heart infusion (BHI) media (Difco Laboratories), diluted 10-fold in fresh BHI, and cultured until OD_{600} = 0.8. *L. monocytogenes* EGD-cGFP (BUG 2539) and L028 (BUG 666) were similarly grown, except that media contained 5 μg/mL chloramphenicol. *Potoroo* kidney epithelial Ptk2 (American Type Culture Collection CCL56) cells were cultured in MEM plus GlutaMAX (GIBCO) supplemented with 1 mM sodium pyruvate (GIBCO), 0.1 mM nonessential amino acid solution (GIBCO), and 10% (vol/vol) FBS. Ptk2 cells were grown at 37 °C and 10% (vol/vol) CO_2.

Infections and Cryopreparation. Holey carbon film-coated gold EM grids (C-flat 2/1-2Au; Protochips, Inc.) were glow-discharged and sterilized on 35-mm diameter Petri dishes under UV light for 15 min. The grids were incubated in MEM at 37 °C and 10% CO_2 for a few hours and then rinsed with fresh medium. Ptk2 cells were then plated on the grids and used 48 h later for the infection assays. *Listeria* was added to host cells at a multiplicity of infection of 10. Infected cells were grown at 37 °C and 10% CO_2 for 2 h, washed with MEM, and incubated with fresh medium for an additional 2 or 3 h. For cryopreparation, we added 15-nm BSA coated colloidal gold on top of the grids, removed excess liquid by blotting from the reverse side, and rapidly plunge-froze the grids in a liquid propane-ethane mixture.

Cryo-Electron Tomography. Cryo-electron tomography (CET) was performed under low-dose conditions using a Tecnai G2 Polara transmission electron microscope (FEI) equipped with a 300-kV field emission gun, a Gatan GIF 2002 postcolumn energy filter, and a 2,048 × 2,048 slow-scan CCD camera (Gatan). The electron microscope was operated at an accelerating voltage of 300 kV, and the pixel size at the specimen level was 0.713 nm. Tilt series were recorded using SerialEM software (1), typically covering an angular range from −55° to +55° with a tilt increment of 1.5°, a defocus of −12 μm, and a total electron dose of 200 electrons per $Å^2$. The applied electron dose for a given tilt angle alpha was proportional to 1/cos(alpha) to compensate for the higher effective specimen thickness at high tilts. The projection images were aligned using the gold beads as fiducial markers. Three-dimensional reconstructions (tomograms) with one time-binned pixel size of 1.42 nm were calculated using IMOD software (2).

Automated Filament Segmentation. We applied an automated segmentation algorithm developed for the tracking of actin filaments, using a generic filament as a template (3). This method can detect filaments in every orientation, including filaments that are parallel to the imaging direction, and thus appear as small cross-sectional spots in a given slice. Tomograms were first subjected to nonlocal means filtering (Fig. S8*A*) and then to template matching using the filament segmentation package implemented in Amira software (FEI) (4). The diameter and length of the cylindrical template were 8 nm and 42 nm, respectively. From the resulting correlation and orientation field maps [more details are provided in the study by Rigort et al. (3)], a similarity function, which evaluates the likelihood that two neighboring voxels belong to the same filament, was calculated. Filaments were traced using threshold correlation values ranging from 0.3 to 0.62, adjusted for each tomogram to provide reliable networks (Fig. S8*B*). Short filaments (<100 nm in comet tails, <70 nm in stress fibers and filopodia) were filtered out to avoid false-negative results due to background noise. When present, the cell wall of the bacterium was extracted from the tomograms using the membrane segmentation method developed by Martinez-Sanchez et al. (5, 6).

Quantitative Data Analysis. Data analysis was performed in the computing platform MATLAB (MathWorks), using as input the coordinates of the automatically detected filaments exported from the Amira software as an ASCII file. The Amira package does not yield equidistant points along a filament [details are provided in the study by Rigort et al. (3)]. To perform the analysis giving the same weight to every point along a filament, the filaments were oversampled at 0.1-nm intervals using a linear interpolation, followed by an undersampling at 3-nm intervals, which is twice the pixel size and close to the Nyquist frequency. Fine sampling steps of 0.1 nm were found to provide the best fit to the original data. Varying final sampling distances between 1 and 4 nm did not affect the results significantly.

Data acquisition for CET is limited to thin areas of the cell. This restricts the movement of the bacteria to a plane, which gives rise to an inhomogeneity in the directions perpendicular to the long axis of the comet tail. Therefore, it was adequate to define the plane of the substrate as the frame of reference. Because the plane of the tomogram reconstruction may deviate from the substrate plane, we used principal component analysis on the coordinates of the resampled filaments to define the substrate plane as the XY plane. The first and the second components were combined such that the Y axis points along the length of the network. The third component defines the Z axis.

We distinguish between filaments that have an inclination smaller than 30° with respect to the XY plane (XY-filaments), which we consider to be included in the XY plane, and filaments with an inclination larger than 30° (Z-filaments). In cases where the motion of the bacterium is not subject to constraints, the definition of XY- and Z-filaments could be generalized to on-axis and off-axis filaments, where the axis is defined as the long axis (Y axis here) of the comet tail. We evaluated the distribution of both XY-filaments and Z-filaments in the XZ plane, projected over the Y axis, as shown in Fig. S8*C*, where the color scale ranges from high occurrence (red) to low occurrence (blue).

To perform nearest neighbor analysis, we determined the local direction of the actin filament at each point along a filament as the tangent of the filament at that point. For each point of a filament, we characterized the closest point of each neighboring filament (within a cube of edge length of 100 nm) by its distance, d (in nanometers), and its relative orientation, α (in degrees), with respect to the reference filament. We represented the occurrences of (d, α) by a 2D histogram (Fig S8*D*); the occurrences along the distance axis are weighted by the distance. The peak occurring at small α indicates the presence of equidistant and nearly parallel filaments.

The projection of the 2D histogram along α results in a histogram of the distances as shown in Fig. S9. Summing up all histograms, but separately for cytoplasmic comet tails, protrusions, stress fibers, and filopodia, provides better statistics to evaluate the mean spacing between parallel filaments for each type of network. We defined a distance range, corresponding to distances with a number of occurrences equal to or higher than 60% of the peak maximum associated with parallel filaments (Fig. S9). This range of spacings between parallel filaments varies

for each type of cellular structure (Table S1). We then evaluated the mean interfilament spacing and the SD in this range.

To explore the local packing of the actin filaments in the networks, we defined a local frame of reference (e1, e2, e3) at every point along a filament. The basis is defined as follows: e2 points in the direction of the actin filament (the tangent of the filament at that point), and e1 points in the direction of the nearest neighbor. If there are several nearest neighbors at similar distance, we chose the neighbor in the vicinity of their center of mass. The e3 frame of reference is defined as the cross-product of e1 and e2. (ξ, η, ζ) are the coordinates of a neighbor position in (e1, e2, e3). We aligned the local frames of reference (e1, e2, e3) of all points along filaments and represented the occurrences of (ξ, ζ) in the e1.e3 plane by a 2D histogram (Fig. S8*E*). The definition of e1 as pointing in the direction of the nearest neighbor yields the red (high intensity) spots in sector III of Fig. S8*E*. Furthermore, it prevents the appearance of an artificial symmetry by ensuring that each neighbor contribution is statistically significant. The asymmetry between the right side (sectors I to V; Fig. S8*H*) and the left side (sectors VII to XI) emerges from finite networks that are not perfectly packed. In the plots shown in Fig. S8*E*, the size of a point is proportional to the number of occurrences in a logarithmic scale, which also defines a red (high occurrence) to blue (low occurrence) color scale.

Our analysis clearly shows that near neighbors tend to be equidistant and arranged into shells (Fig. S8 *D* and *E*). To unveil further the high-order packing of the filaments, we defined three layers. Layer 1 (green; Fig. S8 *D*, *G*, and *H*) corresponds to the range of spacings between parallel filaments evaluated previously (Table S1). Layer 2 (yellow) and layer 3 (red) correspond to twofold and threefold the range of layer 1, respectively. We selected neighbors in layer 1, with a relative orientation α below or equal to 15° with respect to the reference filament. Every point (filament segment) with at least one neighbor satisfying this condition was displayed in black using the Amira software (Fig. S8*F*), highlighting the localization of pairs of closely packed parallel filaments (XY-pairs; Table S1). It should be noted here that pairs were quantified and displayed among XY-filaments because they were absent from Z-filaments.

We defined a bundle as made of at least three parallel equidistant points (filament segments) and a sheet as a planar bundle (i.e., made of three parallel, equidistant filament segments in the same plane). The spatial arrangement of the filaments in a bundle was evaluated as follows. We looked for neighbors in the three layers mentioned above, which belong to a sheet containing the central point (filament segment). The sheet can be of any orientation with respect to the XY plane. Fig. S8*G* shows the occurrences of (ξ, ζ) of the selected neighbors in the e1.e3 plane, for every filament segment centered in (0, 0) (displayed in a gray, filled circle). The point size increases with the number of occurrences in a logarithmic scale, which also defines the color scale. We evaluated the percentage of XY-filaments that belong to a sheet (XY-sheets), as well as the percentage of hexagonally packed bundles (XY-hexagonal bundles) (Table S1). In the latter case, the filament packing, which is commensurate to a hexagonal lattice, was defined by looking for two neighboring filaments in layer 1, which form an equilateral mesh with the central filament segment.

Description of the Spatial Distribution Plots. We observed well-defined populated areas in sectors I, III, V, VII, IX, and XI in the first two to three layers for two filopodia networks (Fig. 3*F* and Fig. S6*E*; two of four tomograms). These filopodia contain up to 6 rotationally arranged neighboring filaments in the first layer, 12 in the second layer, and 18 in the third layer, which pack hexagonally (the number of neighboring XY-filaments are shown in Table S1). In the other two filopodia (Fig. S6*J*), the contribution in sector IX.1 is similar to the contribution in sectors I.1 and V.1 despite the asymmetry in intensity induced by the method, which indicates a stronger contribution of the neighbors on the sides of the central filament (sectors III and IX), rather than in the upper (sectors I and XI) and lower (sectors V and VII) levels. It corresponds to an elementary organization in sheets, followed by hexagonal packing.

In all stress fibers, we observed a stronger contribution of lateral neighbors (sectors III and IX; Fig. 3*H* and Fig. S5 *H* and *J*; eight tomograms) (i.e., stress fibers contain sheets that are placed on top of each other). In some cases, these sheets are hexagonally packed.

Most of the protrusions (Fig. S4 *L* and *N*; seven of nine tomograms) and all cytoplasmic comet tails (Fig. 1*E* and Fig. S2*E*; five tomograms) contain XY-filaments with lateral neighbors (sectors III and IX). In some cases, different (upper and lower) instances were also detected (sectors I and V). In addition, in two of the protrusions, we observed well-defined populated areas in layer 1 in sectors I, III, V, VII, IX, and XI (Fig. 2*E* and Fig. S3*D*), accounting for hexagonally packed bundles as found for two filopodia networks.

1. Mastronarde DN (2005) Automated electron microscope tomography using robust prediction of specimen movements. *J Struct Biol* 152(1):36–51.
2. Kremer JR, Mastronarde DN, McIntosh JR (1996) Computer visualization of three-dimensional image data using IMOD. *J Struct Biol* 116(1):71–76.
3. Rigort A, et al. (2012) Automated segmentation of electron tomograms for a quantitative description of actin filament networks. *J Struct Biol* 177(1):135–144.
4. Stalling D, Westerhoff M, Hege H-C (2005) Amira: A highly interactive system for visual data analysis. *Visualization Handbook*, eds Charles DH, Chris RJ (Elsevier, Butterworth–Heinemann, Burlington, MA), pp 749–767.
5. Martinez-Sanchez A, Garcia I, Fernandez JJ (2011) A differential structure approach to membrane segmentation in electron tomography. *J Struct Biol* 175(3): 372–383.
6. Martinez-Sanchez A, Garcia I, Fernandez JJ (2013) A ridge-based framework for segmentation of 3D electron microscopy datasets. *J Struct Biol* 181(1):61–70.

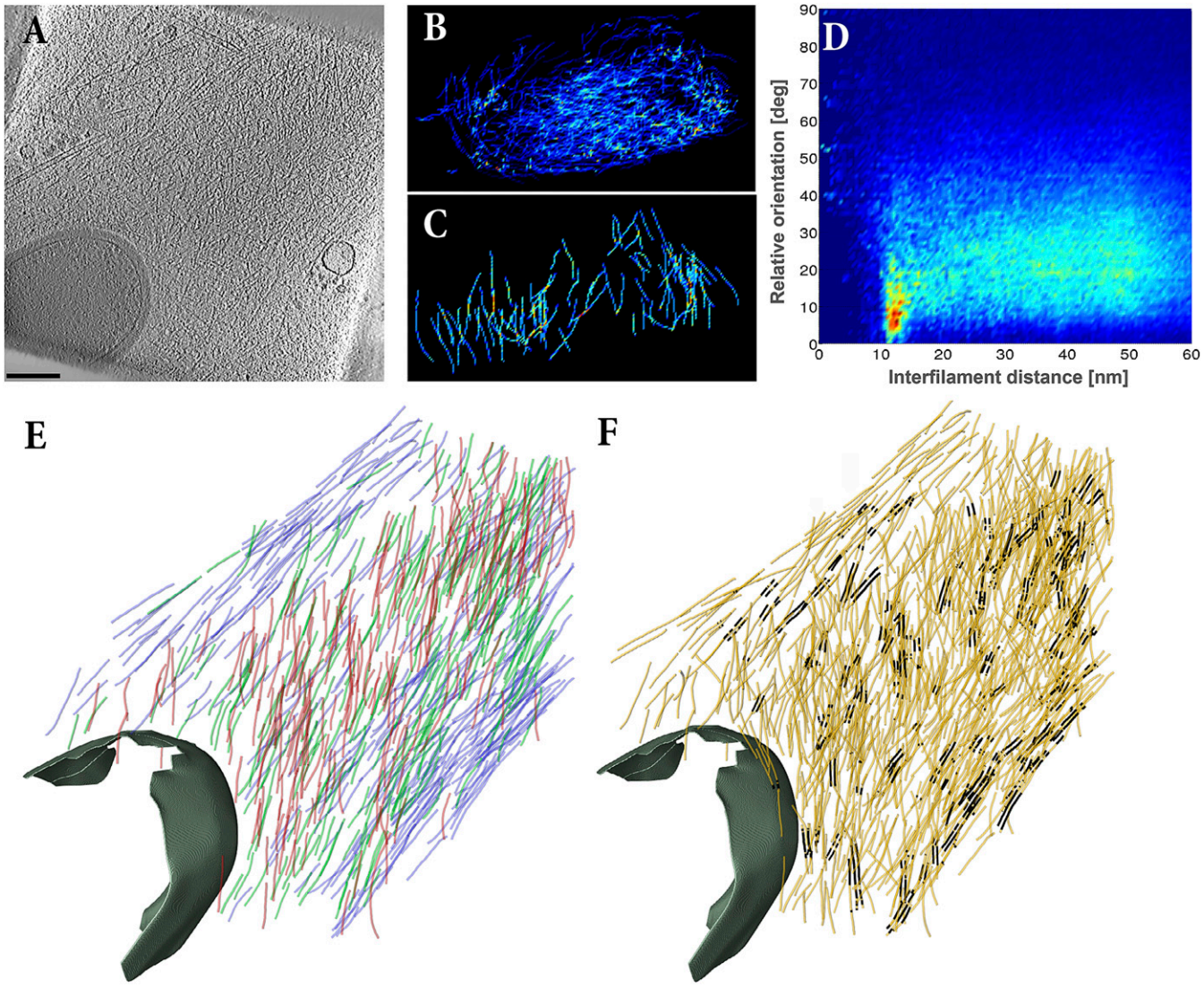

Fig. S1. Densely filled *Listeria* cytoplasmic comet tail contains closely packed parallel filaments. (*A*) Slice through the tomogram of a dense cytoplasmic comet tail in a PtK2 cell infected by *Listeria* EGD-cGFP. (Scale bar: 200 nm.) Distribution of XY-filaments (*B*) and Z-filaments (*C*) in the XZ plane, projected over the Y axis. (*D*) Two-dimensional histogram of interfilament distances, weighted by the distance, and relative orientations between the filaments. (*E*) XY-filaments projected into the XY plane. The color of the filaments corresponds to their angle with respect to the Y axis: 0–15° (blue), 15–30° (green), 30–45° (red). The cell wall of the bacterium is shown in gray. (*F*) XY-pairs of parallel filaments (black) among XY-filaments (orange).

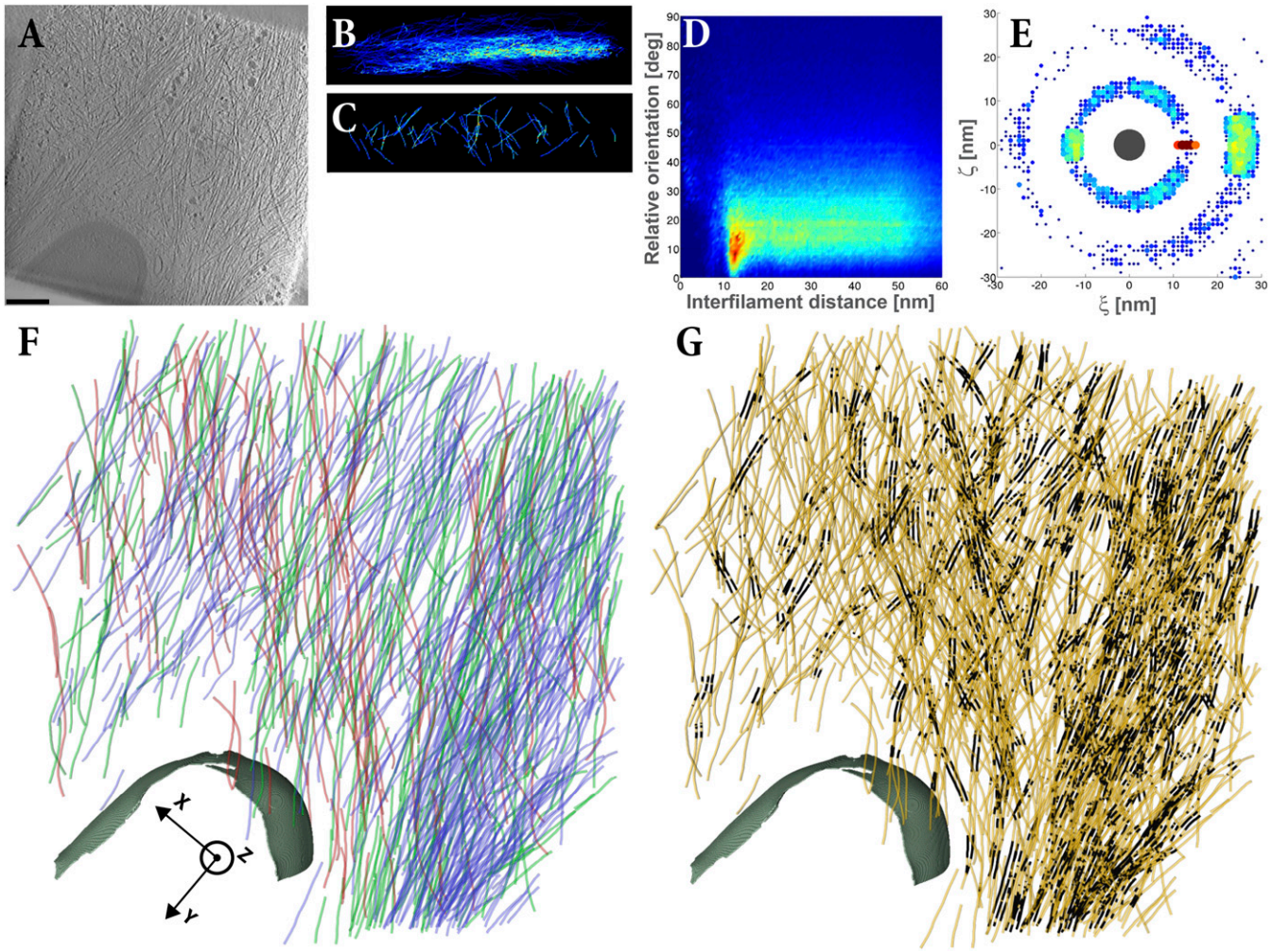

Fig. S2. Densely filled *Listeria* cytoplasmic comet tail shows tightly packed parallel filaments. (*A*) Slice through the tomogram of a dense cytoplasmic comet tail in a PtK2 cell infected by *Listeria* EGD-cGFP. (Scale bar: 200 nm.) Distribution of XY-filaments (*B*) and Z-filaments (*C*) in the XZ plane, projected over the Y axis. (*D*) Two-dimensional histogram of interfilament distances, weighted by the distance, and relative orientations between the filaments. (*E*) Two-dimensional histogram of the (ξ, ζ) coordinates of the neighboring filaments in an XY-bundle in the local plane perpendicular to the central filament (dark gray, drawn to scale). (*F*) XY-filaments projected into the XY plane using the same color code as in Fig. S1*E*. The cell wall of the bacterium is shown in gray. (*G*) XY-pairs of parallel filaments (black) among XY-filaments (orange).

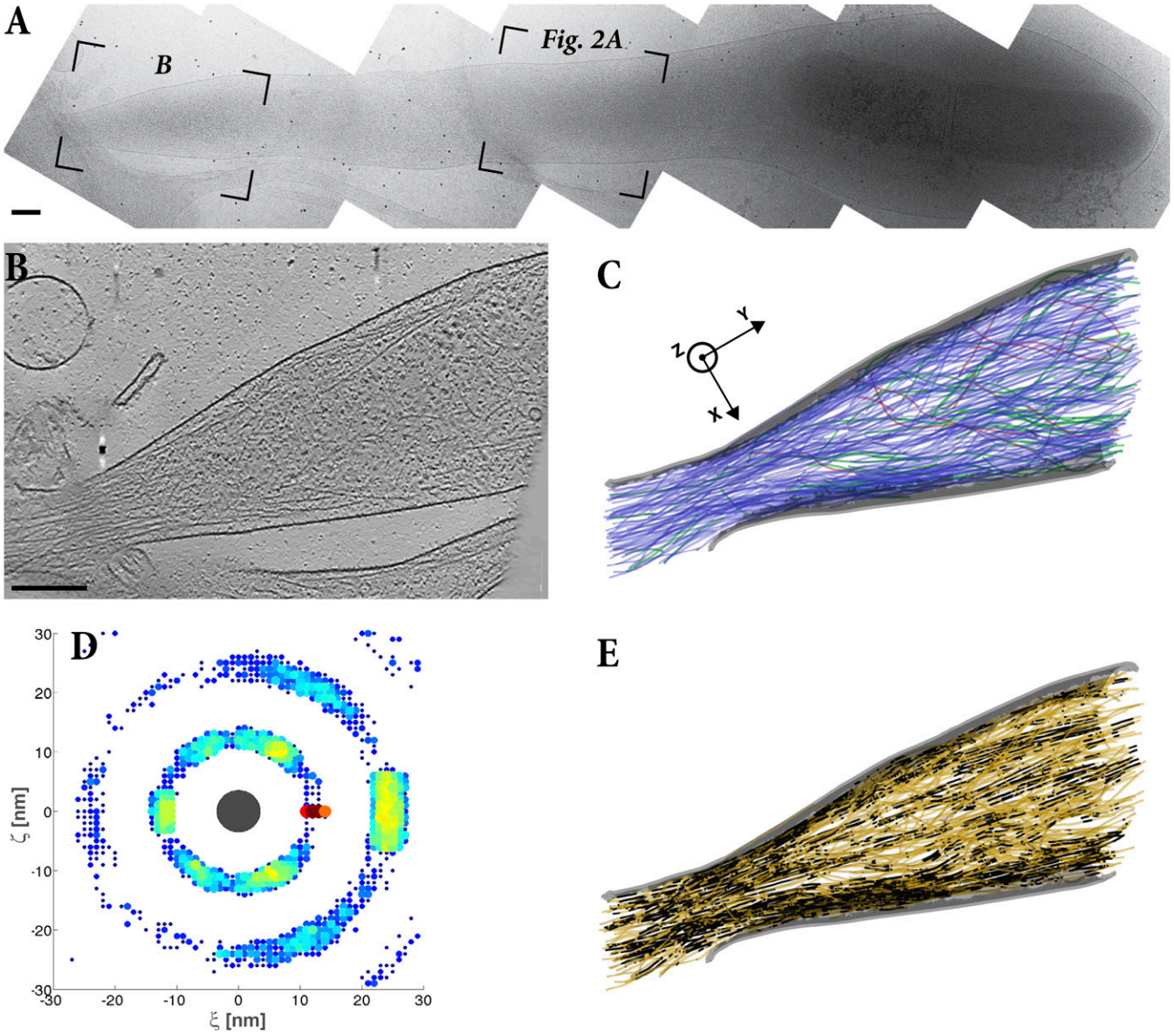

Fig. S3. *Listeria* protrusion shows hexagonal bundles. (*A*) Electron micrograph (stitched projection images) of a protrusion formed by *Listeria* EGD-cGFP at the surface of a PtK2 cell. (Scale bar: 200 nm.) The right box (Fig. 2*A*) indicates the location of the slice through the tomogram shown in Fig. 2*A*. (*B*) Slice through the tomogram at the position indicated by the left box (B) in *A*. (Scale bar: 200 nm.) (*C*) XY-filaments projected into the XY plane using the same color code as in Fig. S1*E*. The plasma membrane of the protrusion is shown in gray. (*D*) Two-dimensional histogram of the (ξ, ζ) coordinates of the neighboring filaments in an XY-bundle in the local plane perpendicular to the central filament (dark gray, drawn to scale). (*E*) XY-pairs of parallel filaments (black) among XY-filaments (orange).

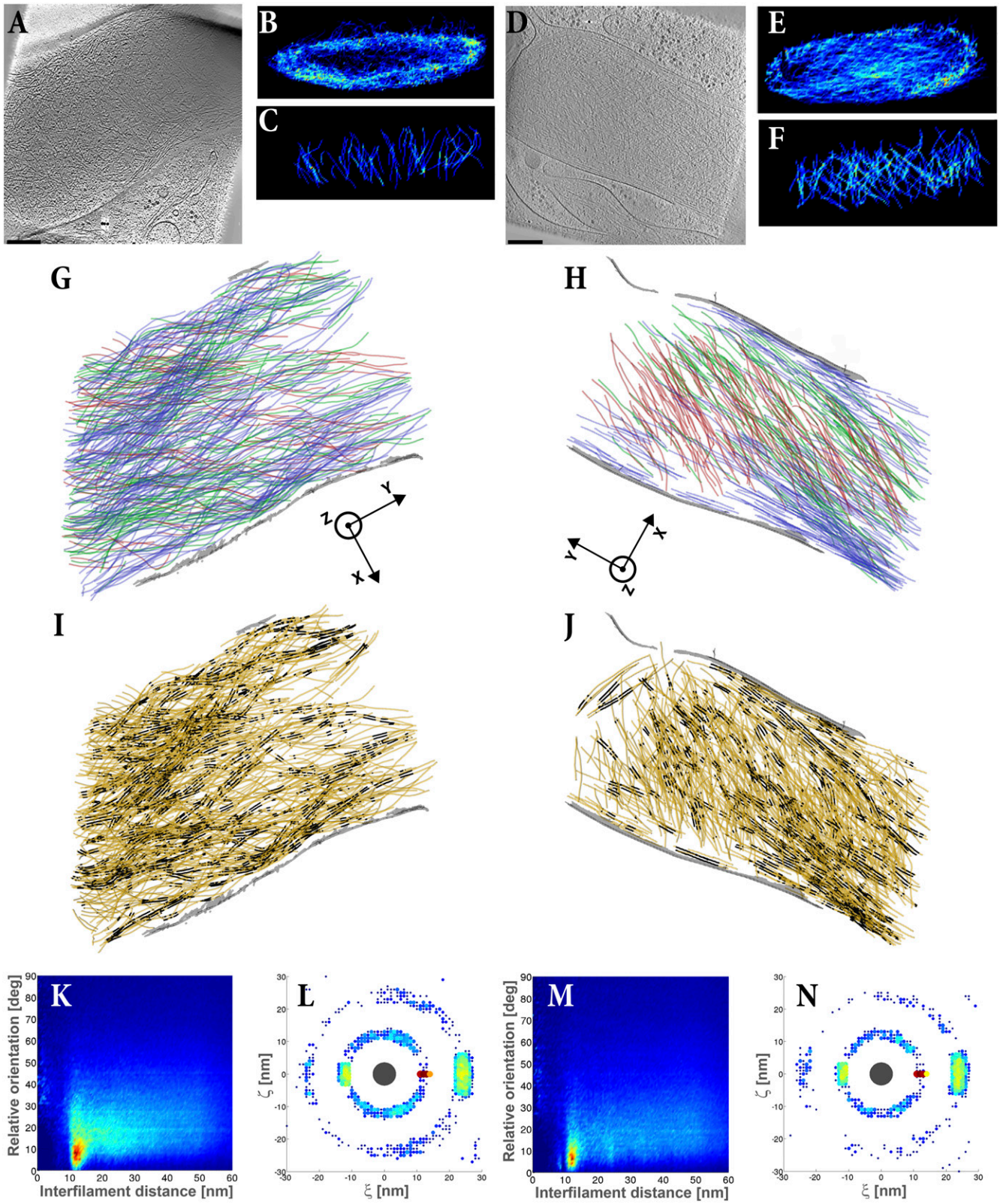

Fig. S4. Hollow and dense *Listeria* protrusions show highly ordered sheets. Slices through the tomograms of hollow (*A*) and dense (*D*) protrusions exiting PtK2 cells infected by *Listeria* EGD-cGFP. (Scale bar: 200 nm). Distribution of XY-filaments (*B* and *E*) and Z-filaments (*C* and *F*) in the XZ plane, projected over the Y axis, for the protrusions shown in *A* and *D*, respectively. (*G* and *H*) XY-filaments projected into the XY plane, extracted from the respective tomograms using the same color code as in Fig. S1*E*. The membrane of the protrusion is shown in gray. (*I* and *J*) XY-pairs of parallel filaments (black) among XY-filaments (orange). (*K* and *M*) Two-dimensional histogram of interfilament distances, weighted by the distance, and relative orientations between the filaments associated with the respective networks. (*L* and *N*) Two-dimensional histogram of the (ξ, ζ) coordinates of the neighboring filaments in an XY-bundle in the local plane perpendicular to the central filament (dark gray, drawn to scale).

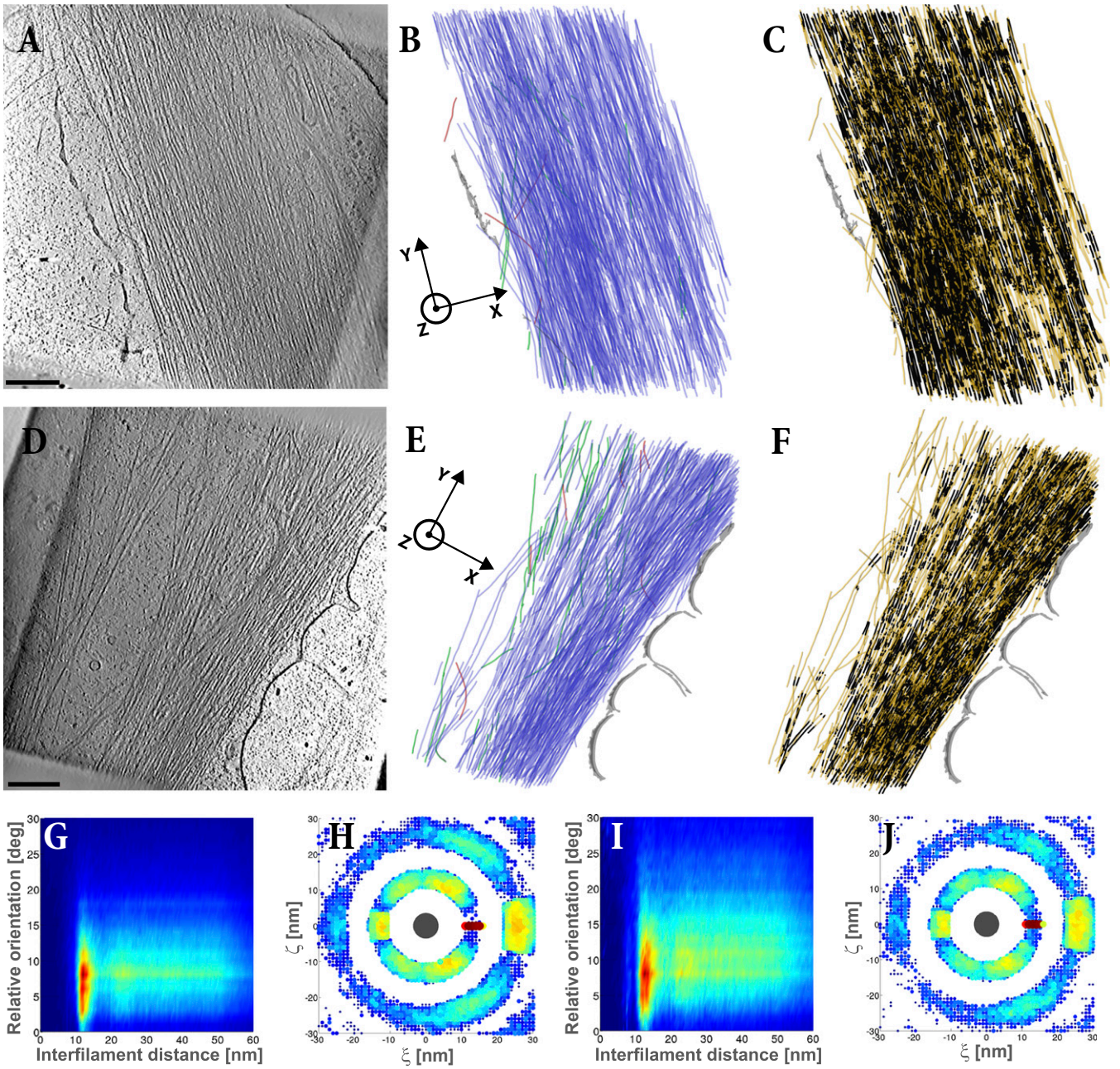

Fig. S5. Stress fibers are made of stacked sheets. (*A* and *D*) Slices through the tomograms of stress fibers in PtK2 cells. (Scale bar: 200 nm.) (*B* and *E*) XY-filaments projected into the XY plane, extracted from the tomograms shown in *A* and *D*, respectively, using the same color code as in Fig. S1*E*. The plasma membrane is shown in gray. (*C* and *F*) XY-pairs of parallel filaments (black) among XY-filaments (orange). (*G* and *I*) Two-dimensional histograms of inter-filament distances, weighted by the distance, and relative orientations between the filaments associated with the respective networks. (*H* and *J*) Two-dimensional histograms of the (ξ, ζ) coordinates of the neighboring filaments in an XY-bundle in the local plane perpendicular to the central filament (dark gray, drawn to scale).

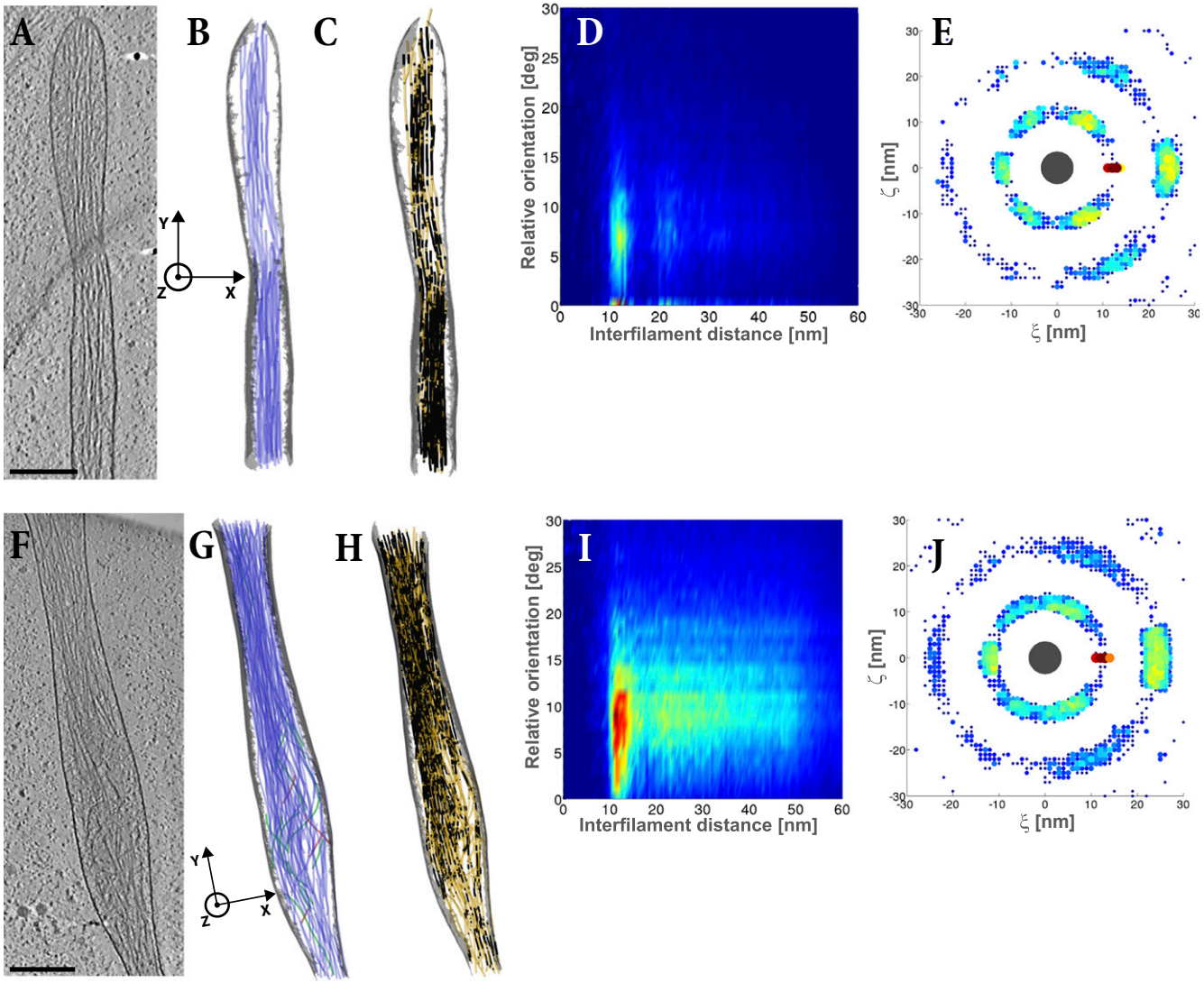

Fig. S6. Filopodia contain hexagonal bundles. (*A* and *F*) Slices through the tomograms of filopodia in PtK2 cells. (Scale bar: 200 nm.) (*B* and *G*) XY-filaments projected into the XY plane, extracted from the tomograms shown in *A* and *F*, respectively, using the same color code as in Fig. S1*E*. The plasma membrane is shown in gray. (*C* and *H*) XY-pairs of parallel filaments (black) among XY-filaments (orange). (*D* and *I*) Two-dimensional histograms of interfilament distances, weighted by the distance, and relative orientations between the filaments associated with the respective networks. (*E* and *J*) Two-dimensional histograms of the (ξ, ζ) coordinates of the neighboring filaments in an XY-bundle in the local plane perpendicular to the central filament (dark gray, drawn to scale).

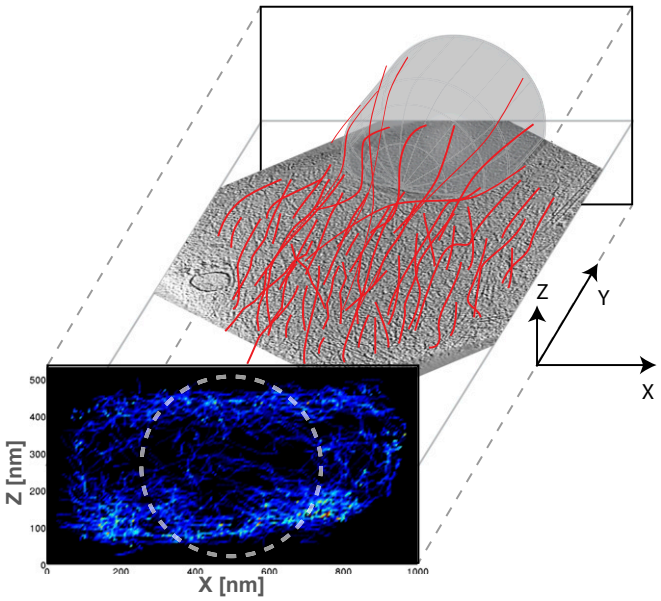

Fig. S7. Scheme illustrates the inhomogeneity of our actin-tail data about the long axis, Y, of the network. Actin filaments are represented in red. A slice through a tomogram of a cytoplasmic comet tail is shown in the XY plane. The cell wall of the bacterium is shown in transparent gray. The filament distribution projected over the Y axis is shown in the XZ plane.

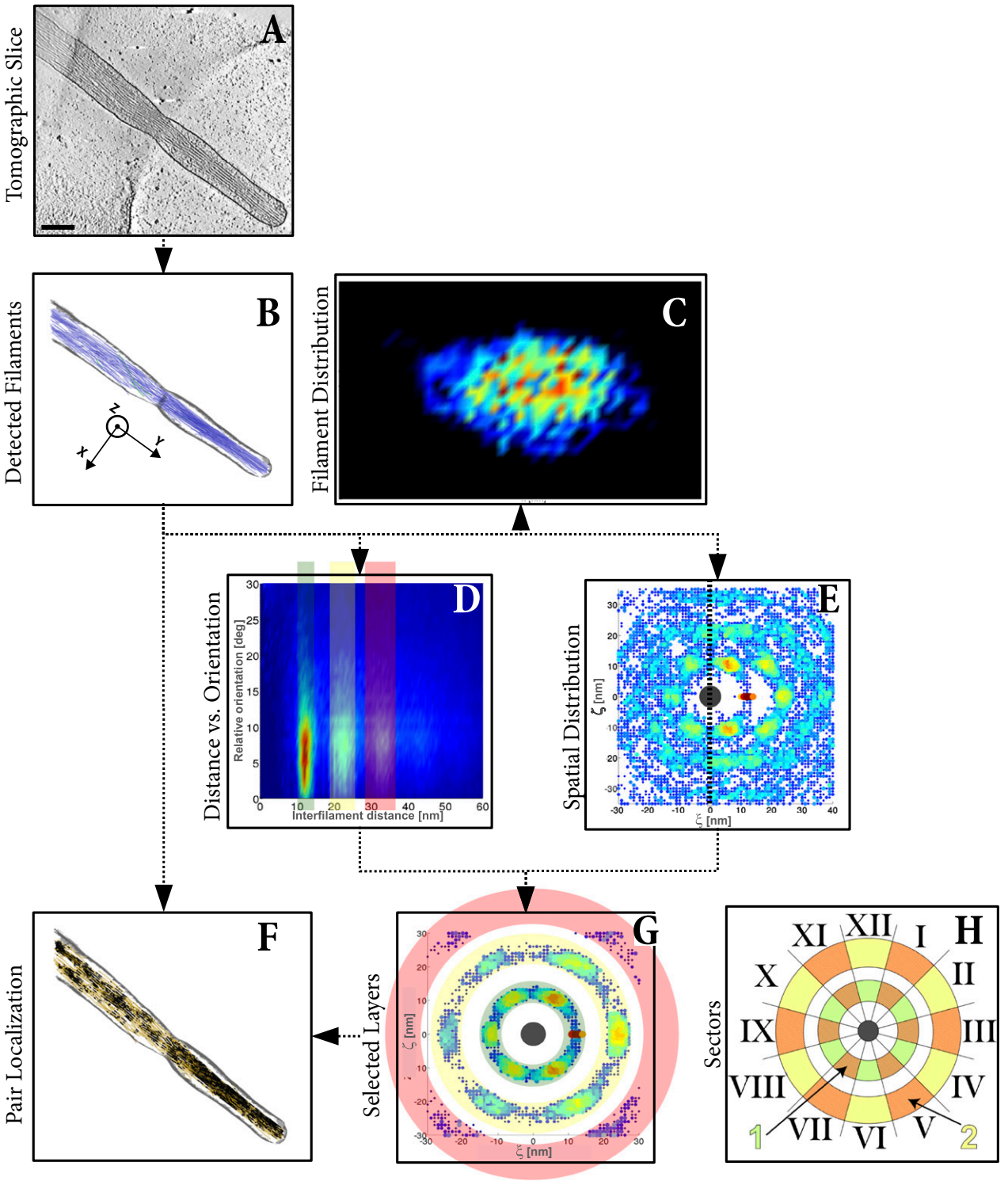

Fig. S8. Work flow to visualize the 3D architecture and the packing of actin filaments on a filopodium dataset obtained by CET. (*A*) Slice through the denoised tomogram of a filopodium. (Scale bar: 200 nm.) (*B*) XY-filaments projected into the XY plane. The color of the filaments corresponds to their angle with respect to the Y axis: 0–15° (blue), 15–30° (green), 30–45° (red). The plasma membrane is shown in gray. (*C*) XY-filament distribution in the XZ plane, projected over the Y axis. The color scale ranges from high occurrence (red) to low occurrence (blue). (*D*) Two-dimensional histogram of interfilament distances, weighted by the distance, and relative orientations between the filaments, with zones of interest highlighted in green, yellow, and red. deg, degrees. (*E*) Two-dimensional histogram of the (ξ, ζ) coordinates of the neighboring filaments in the local plane perpendicular to the central filament (dark gray, drawn to scale). (*F*) XY-pairs of parallel filaments (black) among XY-filaments (orange). (*G*) Two-dimensional histogram of the (ξ, ζ) coordinates of the neighboring filaments in an XY-bundle in the local plane perpendicular to the central filament (dark gray, drawn to scale). Layers 1, 2, and 3 shown in *D* are displayed using the same color code. (*H*) Sectors used as a visual aid to complement the 2D histogram of the filaments belonging to an XY-bundle, as shown in *G*. Layers 1 (green) and 2 (yellow) are also represented. The diameter of the central filament is drawn to scale and displayed in dark gray. The orange area corresponds to the main area of interest observed in our data.

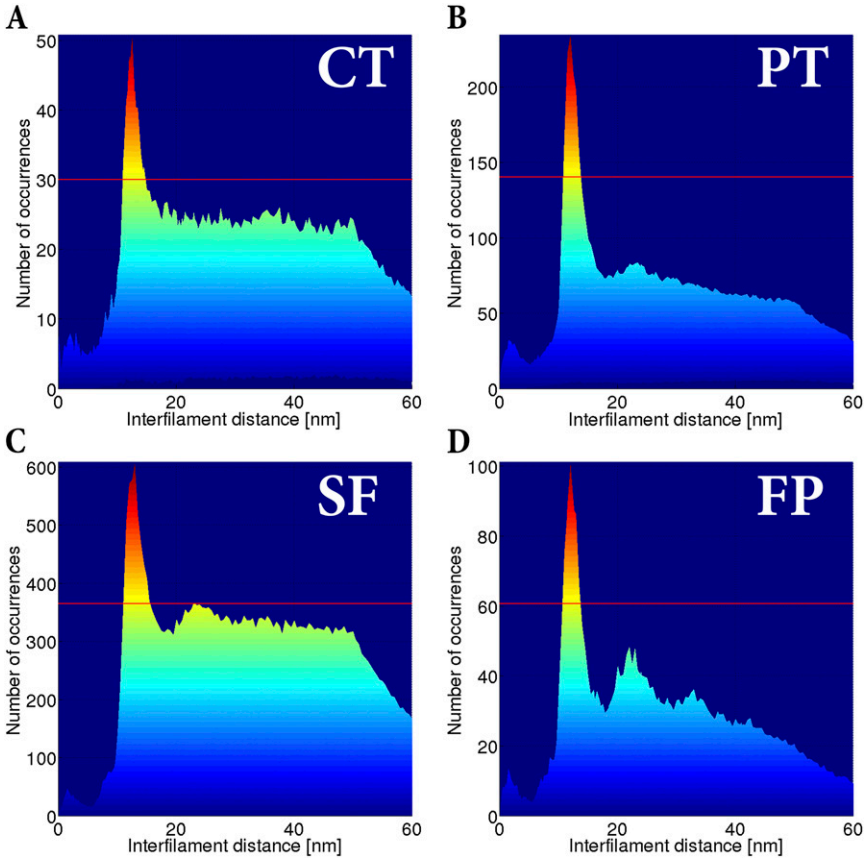

Fig. S9. Distance range criterion for the parallel filaments. Histograms of the interfilament distances, weighted by the distance, in the cytoplasmic comet tail (CT) (*A*), protrusion (PT) (*B*), stress fiber (SF) (*C*), and filopodia (FP) (*D*) overall networks are shown. The red line is drawn at a number of occurrences corresponding to 60% of the peak maximum, defining the most common interfilament spacing. The range includes all distances around the peak, with a number of occurrences above this limit (Table S1).

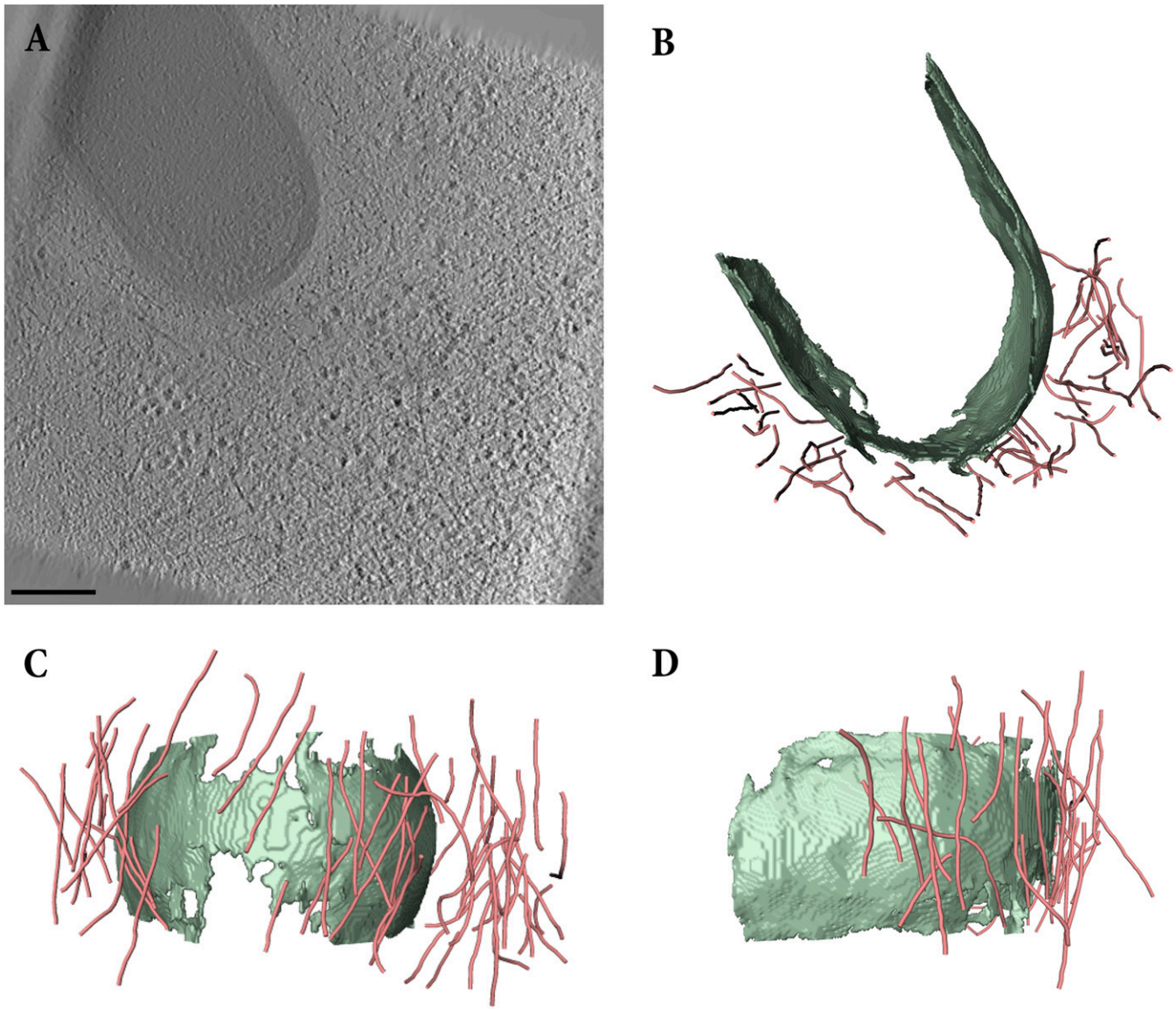

Fig. S10. Actin cloud in the cell interior shows short Z-filaments. (*A*) Slice through the tomogram of a cytoplasmic actin cloud assembled at the surface of *Listeria* EGD (BUG 600) in a PtK2 cell. (Scale bar: 200 nm.) (*B–D*) Top and side views of the Z-filaments (pink) in the actin cloud. The cell wall of the bacterium is shown in green.

Table S1. Parameters of the cellular actin networks

Parameter	Cytoplasmic tails	Protrusions	Stress fibers	Filopodia
N (tomograms)	5	9	8	4
XY-filaments, %	73 ± 15	89 ± 5	98 ± 1	99 ± 1
XY-filaments mean length, nm	170 ± 76	238 ± 133	243 ± 175	337 ± 261
Z-filaments mean length, nm	154 ± 56	153 ± 49	*	*
Parallel filaments range, nm	10.9–14.8	10.8–13.8	11.0–15.6	10.7–13.8
Interfilament spacing, nm	12.8 ± 1.1	12.3 ± 0.8	13.3 ± 1.3	12.2 ± 0.9
XY-pairs range, %	6.8–20.7	11.7–34.8	38.4–63.3	51.1–71.6
XY-pairs mean, %	10.7 ± 5.0	20.0 ± 7.7	48.6 ± 8.6	61.4 ± 8.4
XY-sheets range, %	0.2–2.1	0.7–6.9	5.6–15.8	11.6–24.5
XY-sheets mean, %	0.7 ± 0.7	2.6 ± 2.0	10.3 ± 3.5	17.2 ± 5.5
XY-hexagonal bundles range, %	0–0.8	0.1–6.4	3.3–14.3	9.2–29.8
XY-hexagonal bundles mean, %	0.2 ± 0.3	1.5 ± 2.2	7.4 ± 3.8	18.8 ± 9.2
N (neighboring XY-filaments)	11 ± 6	15 ± 7	30 ± 13	29 ± 8

N (neighboring XY-filaments) is the mean of the number of neighboring XY-filaments per filament. The values of the uncertainties are ±1 SD.
*Not statistically significant.